Gate-tunable Josephson diode in proximitized InAs supercurrent interferometers

Carlo Ciaccia,[1,*] Roy Haller,[1] Asbjørn C. C. Drachmann,[2,3] Tyler Lindemann,[4,5] Michael J. Manfra,[4,5,6,7] Constantin Schrade,[2] and Christian Schönenberger[1,8,†]

[1]*Quantum- and Nanoelectronics Lab, Department of Physics, University of Basel, 4056 Basel, Switzerland*
[2]*Center for Quantum Devices, Niels Bohr Institute, University of Copenhagen, 2100 Copenhagen, Denmark*
[3]*NNF Quantum Computing Programme, Niels Bohr Institute, University of Copenhagen, 2100 Copenhagen, Denmark*
[4]*Department of Physics and Astronomy, Purdue University, West Lafayette, Indiana 47907, USA*
[5]*Birck Nanotechnology Center, Purdue University, West Lafayette, Indiana 47907, USA*
[6]*Elmore Family School of Electrical and Computer Engineering, Purdue University, West Lafayette, Indiana 47907, USA*
[7]*School of Materials Engineering, Purdue University, West Lafayette, Indiana 47907, USA*
[8]*Swiss Nanoscience Institute, University of Basel, 4056 Basel, Switzerland*

(Received 26 March 2023; accepted 28 June 2023; published 25 August 2023)

The Josephson diode (JD) is a nonreciprocal circuit element that supports a larger critical current in one direction compared to the other. This effect has gained growing interest because of promising applications in superconducting electronic circuits with low power consumption. Some implementations of a JD rely on breaking the inversion symmetry in the material used to realize Josephson junctions (JJs), but recent theoretical proposals have suggested that the effect can also be engineered by combining two JJs hosting highly transmitting Andreev bound states in a Superconducting Quantum Interference Device (SQUID) at a small, but finite flux bias. We have realized a SQUID with two JJs fabricated in a proximitized InAs two-dimensional electron gas (2DEG). We demonstrate gate control of the diode efficiency from zero up to around 30% at specific flux bias values which comes close to the maximum of ∼40% predicated in Souto *et al.* [Phys. Rev. Lett. **129**, 267702 (2022)]. The key ingredients to the JD effect in the SQUID arrangement is the presence of highly transmitting channels in the JJs, a flux bias, and an asymmetry between the two SQUID arms.

DOI: 10.1103/PhysRevResearch.5.033131

I. INTRODUCTION

A widely used device in semiconductor electronics is the $p-n$ junction, which is a nonreciprocal element with regards to current flow, able to conduct current primarily in one direction. The presently ongoing rapid scaling of quantum computers will require low-dissipative control electronics that operate close to the quantum chip at low temperatures. These requirements have renewed the question whether there exists a superconducting equivalent of the diode, namely, a device that supports a larger supercurrent in one direction than in another: the Josephson diode (JD) [1,2].

In a conventional Josephson junction (JJ) [3], the current-phase relation (CPR) is sinusoidal $I = I_c \sin(\varphi)$, with I_c being the critical current of the junction and with the ground state corresponding to zero phase bias $\varphi_0 = 0$. For this conventional case, the positive critical current $I_c^+ = \max_\varphi[I(\varphi)]$ is obviously equal to the negative one $I_c^- = |\min_\varphi[I(\varphi)]|$. Since the critical supercurrent is reciprocal, there is no superconducting diode effect (SDE).

A general CPR can have a more complex dependence on the phase [4]. But, in general, $I(\varphi)$ is a 2π-periodic function, and if either time-reversal symmetry or inversion symmetry is preserved, it is an odd function, $I(-\varphi) = -I(\varphi)$ [1]. It can therefore be written as a Fourier series composed of $\sin(k\varphi)$ terms where k is a positive integer and the terms for $k > 1$ are higher harmonics. If higher harmonics are present, the CPR is called nonsinusoidal [5,6]. Such a CPR still does not display a SDE.

A necessary but not sufficient condition for the SDE to occur is that time-reversal symmetry is broken. This can be achieved either by an external magnetic-field of or by means of ferromagnetic elements built into the device. S-F-S junctions, where F (S) denotes a ferromagnet (superconductor), were proposed [7,8] and experimentally studied in various configurations [9–11]. These junctions typically display a π shift in the CPR and are thus know as π junctions. The energy ground state moves from $\varphi_0 = 0$ to $\varphi_0 = \pi$. Despite the presence of a magnetic field and time-reversal symmetry thus being broken, these junctions do not display a SDE.

Both inversion symmetry and time-reversal symmetry are broken in so-called anomalous JJs, also known as φ_0 junctions, where the ground state of the junction has an "anomalous" shift to φ_0 with $0 < \varphi_0 < \pi$ [12]. This situation is achieved in multiband conductors with spin-orbit

*Carlo.Ciaccia@unibas.ch
†Christian.Schoenenberger@unibas.ch

interaction [13–19]. Evidence for φ_0 junctions has been found in experiments with nanowires with strong spin-orbit interaction [20] and in planar Josephson junction arrays [21]. An anomalous JJ is also a necessary condition, but on its own not sufficient. Indeed, a CPR of the form $I(\varphi) = I_c \sin(\varphi - \varphi_0)$ with $0 < \varphi_0 < \pi$ is an anomalous JJ, but still with $I_c^+ = I_c^-$.

The SDE has been observed in materials that display magneto-chiral anisotropy. Here the normal-state resistivity itself depends on the sign of the current density and the sign of the magnetic field [18,22,23]. While this is a small effect in normal metals, it can become large at the transition to a superconducting state [24–26]. Recently, a large SDE was also observed in a 2D $NbSe_2$ superconductor with applied out-of-plane magnetic field [27] and even in field-free situations [1,28,29] including twisted graphene [30–32].

Further studies have also considered, among others, polarized supercurrents, magnetic domain walls, vortex pinning, and combination of *s*-wave and *p*-wave pairing, as well as finite-momentum pairing as the origin of a SDE [33–36]. A SDE was even reported in a scanning-probe microscopy study where a single magnetic impurity was addressed on the surface of a superconductor [37].

Last, topological materials with helical edge states can carry supercurrents with a strong SDE [38–41]. This is evidenced in the highly asymmetric Fraunhofer pattern with the property that $I_c(B) \neq I_c(-B)$, where B is the magnetic field. This arises because of lack of inversion symmetry between the supercurrent flowing along the two edges of the crystal [38]. This situation is very much alike an asymmetric SQUID.

Already in the 1970s, when superconducting interference devices were studied in great detail using tunnel junctions, point contact structures, and Dayem bridges, it was recognized that the critical current of a SQUID can become nonreciprocal [42–45]. The origin was understood to emerge from an asymmetry in the two SQUID arms, but the arms needed to have a nonnegligible loop inductance too. Although the CPR of each single junction was sinusoidal, the CPR became nonreciprocal for the SQUID device due to asymmetric loop inductances.

Today tunable superconductor-semiconductor hybrid devices have become a flourishing research topic [46–50]. In particular, in JJs made of semiconducting weak links, the magnitude of the supercurrent is tunable by local gate electrodes, and, in some devices, the shape of the CPR can be tuned from sinusoidal to highly nonsinusoidal. Consequently, these devices provide a platform for the engineering of the SDE with unprecedented tunability. This has recently been investigated theoretically in Refs. [51,52]. It has been shown that one can achieve a large SDE by combining two nonsinusoidal JJs in a dc-SQUID at finite flux bias even with negligible loop inductances. In this case the nonreciprocal transport $I_c^+ \neq I_c^-$ originates from the interference between higher-order harmonics in CPR of the JJs.

In the current work, we use gate-controlled JJs fabricated in an InAs 2DEG proximitized by an Al layer [53,54]. These rather wide junctions contain many channels with a distribution of transmission eigenvalues. The nonsinusoidal character is due to highly transmissive channels that are present in these devices [55–60]. By tuning the asymmetry between the SQUID arms with the respective gate voltages we show that

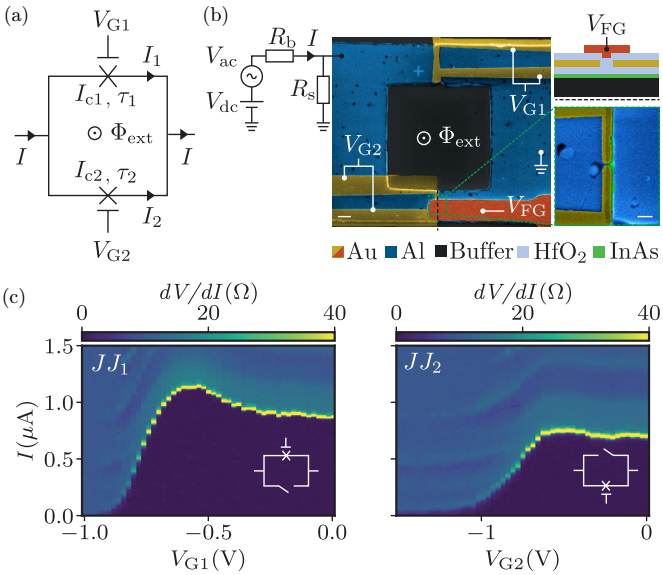

FIG. 1. (a) Circuit schematic of a dc SQUID threaded by the external flux Φ_{ext}, formed by two gate tunable JJs with nonsinusoidal CPRs with critical currents I_{c1}, I_{c2} and transparencies τ_1, τ_2. (b) False-color electron micrograph of the device. The loop consists of a 10 nm Al film (blue) grown on top of an InAs 2DEG (green). The JJs are defined by selectively removing the Al over 150-nm-long stripes on each branch of the loop. Electrostatic gates (yellow and orange) tune the charge carrier density in the junction. We use 15 nm of HfO_2 (light blue) as a gate dielectric. On the right, a zoom-in of JJ_2 is shown before adding the FG. On top, we show a cross-sectional schematic of the gate configuration of JJ_2 along the dashed black line. The scale bar in the main figure is 1 μm, and in the zoom-in it is 300 nm. Dc and ac current bias are defined through the voltage drop over a large series resistor with value $R_b = 1$ MΩ. The SQUID is shunted to ground with a parallel resistor of value $R_s = 10$ Ω. (c) Differential resistance of JJ_1 (left) and JJ_2 (right) as a function of gate voltage and current bias. While one junction is being measured, the other is pinched off. The top junction has a slightly higher critical current due to the different channel widths of $W_1 = 3$ μm and $W_2 = 2.5$ μm.

we can achieve a SDE up to 30%. This comes close to the maximum theoretically predicted value [51].

In Sec. II we present the device geometry, the experimental setup, and the basic characterization of the individual JJs. The nonreciprocal character of the dc-SQUID with JJs having a nonsinusoidal CPR is then shown in Sec. III. We also define an analytical framework with which we are able to distinguish possible origins of the JD effect. Finally, we discuss the measured gate tunability of the diode efficiency in Sec. IV and end with the conclusion in Sec. V.

II. DEVICE AND BASIC PROPERTIES

The circuit diagram of the device is shown in Fig. 1(a), and a colored electron-microscopy picture is presented in Fig. 1(b). The circuit consists of a dc SQUID formed by two planar JJs realized in a shallow InAs 2DEG proximitized by Al layer. The 2DEG is obtained from a quantum well grown on an InP substrate embedded in $In_{0.75}Ga_{0.25}As$ layers of which the top layer is 10 nm thick. The stack is terminated

with an *in situ* grown 10 nm thin Al layer inducing superconductivity in the 2DEG. The SQUID loop and the leads are defined by etching the Al and, additionally, 300 nm deep into the semiconductor stack. The top and bottom Josephson junctions (JJ_1 and JJ_2) in the two branches of the loop are formed by selectively removing the Al in the form of stripes with length $L = 150$ nm and width $W_1 = 3$ μm and $W_2 = 2.5$ μm.

A set of gates, G1, G2, and FG, are used to tune the critical current of the junctions by applying appropriate gate voltages V_{G1}, V_{G2}, and V_{FG}. They are made of two Ti/Au layers, isolated from the Al and from each other by hafnium dioxide (HfO_2) layers. V_{G1} extends over the whole width of JJ_1, while V_{G2} is shaped to gradually deplete JJ_2 laterally, creating a Superconducting Quantum Point Contact (SQPC). An additional gate, V_{FG}, can be used to fine tune the charge carrier density in the SQPC. However, throughout the experiment the QPC functionality is not used and V_{FG} is kept at 0 V.

Our setup sources a current using a 1 MΩ resistor in series to a dc voltage superposed by a small ac component with frequency $f = 17.7$ Hz, supplied by a lock-in amplifier. The ac component has an amplitude of 5 nA. The SQUID is additionally shunted at the source to ground with a resistor $R_S = 10\ \Omega$ directly placed on the sample holder. This shunt resistor has two purposes: (1) it limits the maximum voltage that appears over the junction in the normal state and, thus, the heating and (2) it adds damping to the device avoiding hysteretic switching when assessing the critical current in experiments. We measure the differential resistance of the shunted device using a voltage amplifier and lock-in techniques. In all plots where a measured differential resistance dV/dI is shown the shunt resistor was not subtracted. The measurements presented in the following were obtained with the SQUID device operating in a dilution refrigerator with a base temperature of ∼50 mK.

In Fig. 1(c) we show the measured differential resistance of JJ_1 (left) and JJ_2 (right) as a function of gate voltage and bias current. In the following, we approximate the critical current I_{ci} of the ith junction, $i = \{1, 2\}$, by the current bias value at which the maximum value in differential resistance is measured. Here the bias current is swept from zero to 1.5 μA, looking at transitions from the superconducting to the normal state. From the measurements we extract $I_{ci}(V_{Gi})$. The critical current of both junctions can be tuned from a few nA close to pinch off at negative gate voltages $V_{G(1,2)} \lesssim -1$ V to approximately 1 μA. The key features of these hybrid semiconducting-superconducting JJs are the gate tunable critical current and the nonsinusoidal CPR.

In the short-junction limit, i.e., for junctions with a length L shorter than the superconducting coherence length ξ in the normal metal, the zero temperature limit of the supercurrent $I(\varphi)$ is given by [5]

$$I(\varphi) = \sum_j \left(\frac{\tau_j e\Delta}{\hbar}\right) \frac{\sin(\varphi)}{\sqrt{1 - \tau_j \sin^2(\varphi/2)}}. \tag{1}$$

Here τ_j is the transmission probability per channel j. In multichannel devices with disorder, a universal distribution function of transmission eigenvalues was obtained [55,61–63]. The distribution is bimodal with many low transmissive channels that contribute little to the current, but also with some channels having a transmission probability close to 1. These high-transmissive channels lead to the overall nonsinusoidal character. This is approximated with an effective (but constant) transmission probability τ^* per channel and written as a single-channel nonsinusoidal CPR given by

$$I(\varphi) = \frac{I_c}{A_N} \frac{\sin(\varphi)}{\sqrt{1 - \tau^* \sin^2(\varphi/2)}}. \tag{2}$$

For the later discussion of the measurements the critical current I_c of the junction and a unitless normalization parameter A_N are introduced. The ratio I_c/A_N is given by $N\tau^* e\Delta/\hbar$ with N the number of channels. Note, for the single junction we have $I(-\varphi) = -I(\varphi)$ and thus $I_c^+ = I_c^- = I_c$. It is also seen that for small values of τ^* the CPR approaches a sinusoidal dependence. From experimental $I(\varphi)$ curves, we deduce the critical current I_c of each junction, τ^* and A_N. Note that only two parameters are independent.

As shown in Fig. 1(a) the total supercurrent I across the SQUID is the sum of the currents flowing in both branches I_1 and I_2 through the two JJs:

$$I(\varphi_1, \varphi_2) = I_1(\varphi_1) + I_2(\varphi_2). \tag{3}$$

The two junctions are described by I_{c1}, I_{c2} and τ_1^*, τ_2^*. The uniqueness of phase around the loop leads to the so-called fluxoid relation (modulo 2π),

$$\varphi_1 - \varphi_2 = 2\pi\, \Phi_{ext}/\Phi_0 = \varphi_{ext}, \tag{4}$$

where Φ_{ext} denotes the externally induced flux, $\Phi_0 = h/2e$ the superconducting flux quantum, and φ_{ext} the respective phase. In this form of the fluxoid relation the loop inductance has been neglected. For a finite loop inductance there is an additional flux contribution which depends on the currents I_1 and I_2 flowing in each arm. It has been shown that asymmetric loop inductances can also induce a superconducting SDE [45,64,65]. To estimate the role of loop inductances in our experiment we perform a full analysis with equations given in the Appendixes, specifically in Appendix E. Taking Eq. (3) and Eq. (4) together yields an effective superconducting junction with a CPR:

$$I(\varphi) = I_1(\varphi) + I_2(\varphi - \varphi_{ext}). \tag{5}$$

For a simple sinusoidal CPR, the addition of the two terms yields a φ_0 junction without a SDE, even when the two JJ have different critical currents. In contrast, in the presence of higher order harmonics, which appear for a nonsinusoidal CPR, constructive and destructive interference effects, acting opposite for the two current bias directions, give rise to unequal critical currents $I_c^+ \neq I_c^-$ and thus to a SDE [51,52].

III. JOSEPHSON DIODE EFFECT

Figure 2(a) shows the differential resistance of the SQUID as a function of current bias and perpendicular magnetic field $B_\perp$, the latter providing the flux Φ_{ext} through the SQUID loop. We have chosen a gate configuration with $V_{G1} = V_{G2} = 0$ V for which the two critical currents are similar: $I_{c1} = 0.87$ μA and $I_{c2} = 0.67$ μA. A clear SDE is visible. For example, at the place of the orange arrow, we obtain $I_c^+ = 0.64$ μA and $I_c^- = 0.4$ μA.

In this experiment, the current bias is swept from negative to positive values. This means that we measure the positive

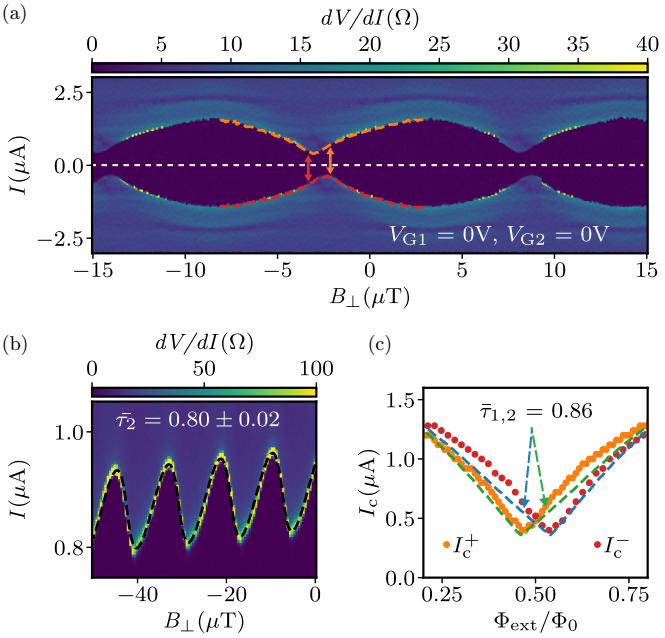

FIG. 2. (a) SQUID oscillations with $V_{G1} = V_{G2} = 0$. The critical current I_c^+ and the retrapping current I_r^- over one flux period are highlighted in orange and red, respectively. At fixed magnetic field, the absolute value of the critical current in the two sweep directions is not the same. This is best seen in the region $-5 < B_\perp < 0$ μT with a visible example taken at the red and orange arrows, where the SDE has a magnitude of ∼23%. (b) Measurement for a strongly asymmetric SQUID setting with $V_{G1} = 0$ V and $V_{G2} = -1.1$ V. The junction with the large critical current JJ_1 serves as the reference junction. As a consequence, the critical current as a function of flux now reflects the CPR of the weaker junction JJ_2. The CPR is strongly nonsinusoidal, and a fit (black dashed line) yields $\tau_2^* = 0.8$. (c) Plot of the extracted I_c^+ (orange) and I_c^- (red) taken from the measurement in (a) and from a measurement where we sweep the current bias from positive to negative values (see Appendixes). The dashed two curves (green and blue) show simplified model fits with $\tau_{1,2}^* = 0.86$ and the critical currents of the junctions taken from Fig. 1(c).

switching current I_c^+, but on the negative side, we actually measure what is called the retrapping current I_r^- where the device switches from the normal to the superconducting state. Due to dissipation, the junction can overheat in the normal state giving rise to a hysteresis between the switching and retrapping currents with the retrapping current being smaller in magnitude than the switching current. This would result in an artificial SDE. To exclude this, we have measured the same plot as in Fig. 2(a) but sweeping now from positive to negative bias currents. The comparison shows (see Appendix C) that the hysteresis between retrapping and switching currents is small and can be neglected. Physically, this is the case due to the low shunt resistant of $R_s = 10\ \Omega$, which limits the voltage over the junction to <25 μV and, thus, limits the heating.

Another strong argument against an artificial effect is seen in Fig. 2(a) when one looks at the switching values at the place of the red arrow, where $I_c^+ = 0.44$ μA and $I_r^- = 0.6$ μA. Here the sign of the SDE is reversed, $I_c^+ < I_r^-$. This cannot be explained by a hysteresis between the switching and retrapping currents, since the retrapping current should always be smaller than the switching current.

As introduced before, a contribution from loop inductances may generate the SDE too, if the loop inductances in the two arms are different. Applying finite element simulations (Appendix B), we obtain $L_1 \approx 39$ pH and $L_2 \approx 44$ pH. The relative phase shift between the two SQUID arms due to the loop inductances at a bias current $I = 1$ μA is only $\frac{2\pi}{\Phi_0}(L_2 - L_1)I \sim 0.03$ rad and gives a small contribution to the SDE. We properly simulate the effect of the loop inductances on the critical current of the SQUID in Appendix F and find that the loop inductances alone cannot explain the observed SDE in our experiment.

We also note that the measured CPR of the SQUID in Fig. 2(a) is periodic with a periodicity of 11.6 μT. Since this should correspond to an added flux quantum Φ_0 in the area A_h of the inner SQUID hole, we obtain for $A_h = 175\ \mu m^2$. This is approximately a factor of 2.3 bigger than the geometrical area defined by the etched square-shaped hole of size 75 μm^2. This discrepancy can be attributed to the flux-focusing effect [66]. The magnetic field above the superconductor is screened by the Meissner effect leading to an enhanced magnetic field within the inner hole. The enhancement factor can be estimated by the ratio of the outer superconducting loop area of $\approx 150\,\mu m^2$ relative to A_h, which yields a factor of 2 in good agreement with the experiment.

In a sufficiently asymmetric SQUID configuration one can measure the CPR of the weak junction alone [6]. Figure 2(b) shows a measurement of the CPR of a single junction, obtained during the same cool down. Here $V_{G1} = 0$ V and $V_{G2} = -1.1$ V so that the current in JJ_1 is large ∼0.9 μA and in JJ_2 it is small ∼0.1 μA. In such a situation JJ_1 acts as reference junction, and the critical current of the weak junction JJ_2 can be obtained from Eq. (5) as

$$I_c^+ = \max_\varphi [I_1(\varphi) + I_2(\varphi - \varphi_{ext})], \tag{6}$$

$$I_c^+(\varphi_{ext}) \simeq I_{c1} + I_2(\tilde{\varphi}_1 - \varphi_{ext}), \tag{7}$$

where $\tilde{\varphi}_1$ is the phase value for which JJ_1 has its maximal value I_{c1}. Hence, we see that under the condition that the reference junction dominates, we obtain the phase dependence of the critical current of the weak junction from the flux dependence of the critical current of the SQUID. Applying Eq. (2) to fit the measured data yields for the effective transmission probability $\tau^* = 0.8 \pm 0.02$. This is a large value, showing that the CPR is strongly nonsinusoidal, something that is visibly seen in the graph of Fig. 2(b). If one makes use of the universal bimodal distribution function of transmission eigenvalues to determine τ^* [55,61–63], one obtains $\tau^* = 0.866$. Including different devices nominally fabricated the same way, we always find a large effective transmission value of order ∼0.8 in agreement with theoretical expectations for a multichannel disordered junction in the short junction limit.

In Fig. 2(c) we compare the oscillations of I_c^+ and I_c^- as a function Φ_{ext} with the simplified model of Eq. (5). We take the measured critical currents of the two junctions as input parameters, $I_{c1} = 0.87$ μA and $I_{c2} = 0.67$ μA, and assume $\tau_1^* = \tau_2^* = \tau^*$ as a single fitting parameter. The best agreement is obtained for $\tau^* = 0.86$. We note that a similar model

TABLE I. Conditions for obtaining a SDE (DE). An extended table that includes the loop inductances can found in Appendix G. The first column is used to distinguish the classical sinusoidal CPR ($\tau^* = 0$) from a strongly skewed CPR described by a highly transmissive ballistic A JJ with an effective transmission probability $\tau^* > 0$. $\alpha(\beta)$ denotes the asymmetry in critical currents (transmission probabilities) of the two junctions.

τ^*	α	β	SDE
0	0	n.a.	No
0	$\neq 0$	n.a.	No
$\neq 0$	0	0	No
$\neq 0$	0	$\neq 0$	Yes
$\neq 0$	$\neq 0$	0	Yes
$\neq 0$	$\neq 0$	$\neq 0$	Yes

calculation based only on loop inductances barely matches the measurement. It is shown as a comparison in Appendix F.

The fits for I_c^+ (green) and I_c^- (blue) reproduce the relative shift along the flux axis very well. The shape of the curves is, however, not reproduced so well. In the region $\Phi_{ext}/\Phi_0 \in [0.25, 0.5]$ and $\Phi_{ext}/\Phi_0 \in [0.5, 0.75]$ respectively, the measured I_c^+ and I_c^- curves are higher than what is obtained with the model. Deviations between the experimental and the modeled curves could be attributed to the choice of CPR used in the model. First, we considered an average transparency instead of a distribution of transparencies. Second, the expression of the current carried by the Andreev bound states could be different from Eq. (2), since our junctions could be in a regime intermediate to the short and long junction limit. And, in the third place, spin-orbit effects may affect the CPR too. For junctions of similar length in the same material system, it has been shown that spin-orbit interaction splits the ABS into spinful states with different dispersion relations [67]. Noticeably, the experiment indicates that these deviations result in an increase of the SDE compared to what is predicted by the simple model.

Having established that a SDE appears in a SQUID with junctions having a nonsinusoidal CPR with asymmetry, we summarize in Table I the necessary conditions for the SDE (DE). To describe the asymmetry we introduce two asymmetry parameters α and β for the critical currents and the effective transmission probabilities, respectively:

$$\alpha = \frac{I_{c1} - I_{c2}}{I_{c1} + I_{c2}} \quad \text{and} \quad \beta = \frac{\tau_1^* - \tau_2^*}{\tau_1^* + \tau_2^*}. \tag{8}$$

An extended table, which also considers the effect of loop inductances, is presented in Appendix G. It shows that the diode effect appears when the SQUID arms are asymmetric. The only exception is for sinusoidal JJs, where an asymmetry in the critical currents in not enough to produce a diode effect.

IV. GATE TUNABLE DIODE EFFICIENCY

The SDE can be quantified via the diode efficiency, defined as

$$\eta = \frac{I_c^+ - I_c^-}{I_c^+ + I_c^-}. \tag{9}$$

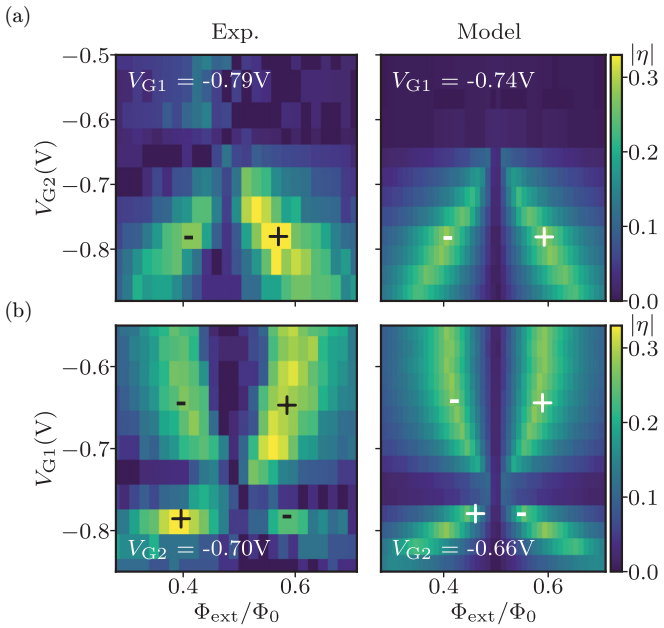

FIG. 3. Magnitude of the diode efficiency $|\eta|$ as a function of external flux Φ_{ext} for different gate configurations as obtained from the measurements (left) and as calculated from the model (right). The sign of η is indicated on the visible lobes with + and −. The model takes into account the numerically simulated loop inductances, their asymmetry, and the values $I_{c(1,2)}$ of the two junctions obtained from the measurements in Fig. 1(c). The JJ transparencies were fixed to $\tau_1^* = \tau_2^* = 0.86$. (a) $|\eta|$ as a function of V_{G2} at fixed V_{G1}, and (b) $|\eta|$ as a function of V_{G1} at fixed V_{G2}. Note that for $\Phi_{ext}/\Phi_0 = 0.5$, which equals $\varphi_{ext} = \pi$, $\eta = 0$ independent on any other parameters.

In Fig. 3 we show the magnitude of the diode efficiency $|\eta|$ as a function of external flux Φ_{ext}/Φ_0 for different gate configurations as obtained from the experiment (left) and as calculated from the model (right). In the model we make use of the relation between critical current and gate voltage of the individual junctions $I_{ci}(V_{Gi})$ and use these values as input parameters in the first approximation. We also use the simulated loop inductance values from which we obtain the phase response due to screening $\varphi_L = 4\pi \bar{I}_c \bar{L}/\Phi_0$, the loop inductance asymmetry $\gamma = (L_1 - L_2)/(L_1 + L_2)$ with L_1, L_2, and $\bar{I}_c$ and $\bar{\tau}^*$ the respective mean values. We assume that the effect of the gate voltage is mainly to change the critical current value I_{ci} through the number of channels N, while τ_i^* roughly stays constant. We fix $\tau_1^* = \tau_2^* = 0.86$, but we note that the calculated η plot is insensitive if one varies τ_2^* between 0.8 and 0.9.

In Fig. 3(a) we plot $|\eta|$ for different values of V_{G2} at fixed V_{G1}. Both in the experiment and in the model, $|\eta|$ drops for $-0.7 < V_{G2} < -0.5$ V. As seen in Fig. 1(c), this corresponds to a gate configuration with $I_{c1} \approx I_{c2}$, so that $\alpha \approx 0$. As expected, the absence of critical current asymmetry decreases the diode efficiency. To obtain in the model the same diode efficiencies η as measured, we had to increase the critical current of JJ_1. In the experiment, we had V_{G1} fixed at −0.79 V, which would correspond to $I_{c1} = 470$ nA. However, in order to match the model with the data, we had to use 710 nA, corresponding to $V_{G1} = -0.74$ V, as indicated in the top left

corner of the figure. Without this correction, the measured $|\eta|$ values would have been larger than what the model predicts. We attribute this difference in gate voltage to gate jumps that occur from time to time. We note that there are days between the measurements in Fig. 1(c) and Fig. 2(a).

In Fig. 3(b) we show the dependence of $|\eta|$ as a function of V_{G1} at fixed $V_{G2} = -0.7$ V. As before, to match the model to the experiment, we had to increase I_{c2} from the initially measured value of 590 nA at V_{G2} to 650 nA, which correspond to I_{c2} measured at $V_{G2} = -0.66$ V.

Both in the experiment and in the model one can observe the typical butterfly pattern of η as predicted in Ref. [51]. The two arms of maximum $|\eta|$ meet at the point of minimum asymmetry at $\Phi_{ext}/\Phi_0 = 0.5$ for $V_{G2} \approx -0.65$ V and $V_{G1} \approx -0.75$ V for Fig. 3(a) and Fig. 3(b) respectively, where η drops to 0.

The model qualitatively reproduces the gate dependence of the diode efficiency very well. We obtain a maximum $|\eta|$ of $\simeq 0.3$ from the experiment. This 30% efficiency is much larger than what has previously been obtained in a SQUID with asymmetric loop inductance [68]. Taking a SQUID model with a single channel JJ junction, we numerically find for the maximum efficiency $\eta = 0.37$. This is obtained for $\tau_1 = 1$ and $\tau_2 = 0.75$ or the reverse. This could be achieved by combining a single channel ballistic $\tau = 1$ Josephson junction realized in atomic contacts [6] with a semiconductor-superconductor hybrid device as we have discussed here.

V. CONCLUSION

In conclusion, we have investigated the origin of the superconducting diode effect (SDE) in a supercurrent interferometer realized in a proximitized InAs quantum well stack. We show that in such a system the SDE can originate from the nonsinusoidal character of the JJs, and hence, reflecting a subtle interference between higher-order harmonics of the CPRs of the individual JJs. In addition to higher harmonics, an asymmetry either in the composition of the Fourier components in the CPR or in the critical current of the two JJ, and a finite flux bias $\varphi_{ext} \neq \{0, \pi\}$ is required to obtain a SDE. These conditions ensure that time-reversal symmetry and inversion symmetry are both broken. A similar conclusion was drawn by a recent experimental study in three terminal devices, where a SDE was realized [69]. Future directions include the possibility to concatenate more SQUIDs in parallel in order to further increase the diode efficiency as was proposed in Ref. [51].

All data in this publication are available in numerical form [71].

Note. Recently we became aware of a similar study in a dc SQUID realized in a Ge quantum well structure [70].

ACKNOWLEDGMENTS

We thank C. M. Marcus for his support in initiating this work and collaboration. This research was supported by the Swiss National Science Foundation through Grants No. 172638 and No. 192027 and the QuantEra project SuperTop. We further acknowledge funding from the European Union's Horizon 2020 research and innovation program: from the European Research Council (ERC) Grant Agreement No. 787414, ERC-Adv TopSupra; Grant Agreement No. 828948, FET-open project AndQC; Grant Agreement No. 847471, project COFUND-QUSTEC; and Grant Agreement No. 862046, project TOPSQUAD. Constantin Schrade acknowledges support from the Microsoft Corporation, and Christian Schönenberger from the Swiss Nanoscience Institute (SNI).

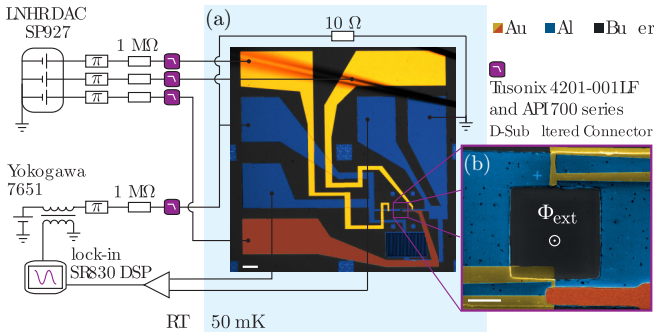

FIG. 4. (a) False color optical image of the full device together with a sketch of the measurement setup. The scale bar is 100 μm. (b) Zoom-in over the SQUID showing the loop area threaded by the external flux Φ_{ext}. The electron density in the junction region is tuned via a set of gates coloured in yellow and brown. The scale bar is 3 μm.

APPENDIX A: FABRICATION AND MEASUREMENT SETUP

The wafer used in this experiment was grown by molecular beam epitaxy (MBE). The stack consists from bottom to top of an InP substrate, a 1-μm-thick buffer realized with $In_{1-x}Al_xAs$ alloys, a 4 nm $In_{0.75}Ga_{0.25}As$ bottom barrier, a 7 nm InAs layer, a 10 nm $In_{0.75}Ga_{0.25}As$ top barrier, two monolayers of GaAs acting as a stop etch layer, and 10 nm of Al deposited *in situ* without breaking the MBE vacuum. The two-dimensional electron gas is characterized from a Hall bar device and shows a peak electron mobility of $\mu = 12\,000$ cm^2 V^{-1} s^{-1} for an electron density of 16×10^{11} cm^{-2}, corresponding to an electron mean-free path of $l_e \approx 230$ nm.

The device is fabricated using standard electron beam lithography techniques. The MESA is electrically isolated by first removing the top Al film with Al etchant Transene D, followed by a deep III–V chemical wet etch with H_2O:$C_6H_8O_7$:H_3PO_4:H_2O_2 (220:55:3:3). Next, the Al film on the MESA is selectively etched with Al etchant Transene D to define the planar JJ. Electrostatic gates are made of two Ti/Au layers, isolated from the Al and from each other by hafnium oxide (HfO_2) layers grown by atomic layer deposition (ALD) at a temperature of 90 °C over the entire sample. The first layer of gates is made of electron-beam evaporated Ti/Au (5 nm/25 nm) on top of 15 nm HfO_2. Connections to the external circuit are obtained by evaporating Ti/Au (5/85 nm) leads at ±17° to overcome the MESA step. A second layer of gates, made of angle-evaporated Ti/Au (5/85 nm), is patterned on top of 25 nm of HfO_2.

Measurements are carried out in a Triton 200 cryogen-free dilution refrigerator with a base temperature of ≈50 mK. An overview of the measurement setup is shown in Fig. 4. The

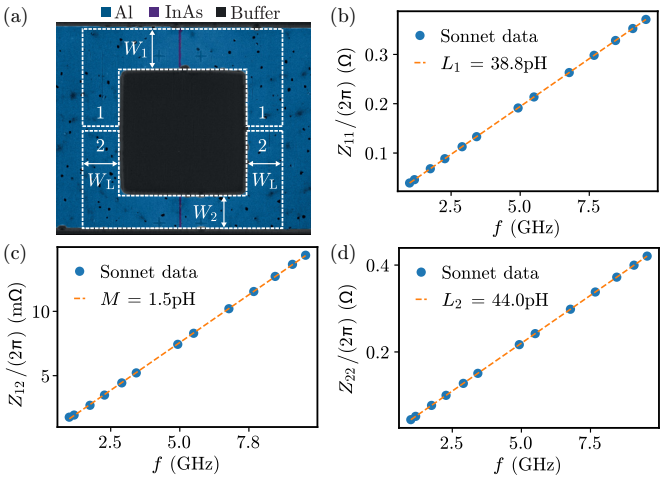

FIG. 5. Sonnet simulations of the loop inductances. The superconducting loop is segmented into an upper (lower) branch 1 (2) indicated by the white dashed boxes. The respective width are $W_1 = 3$ μm, $W_2 = 2.5$ μm, and $W_L = 2.75$ μm. The two inductances L_1, L_2 and the mutual inductance M are deduced from the slope of the frequency dependent two-port impedances. It is seen that $M \ll L_{1,2}$ and that there is a small asymmetry of ∼6% in the loop inductances.

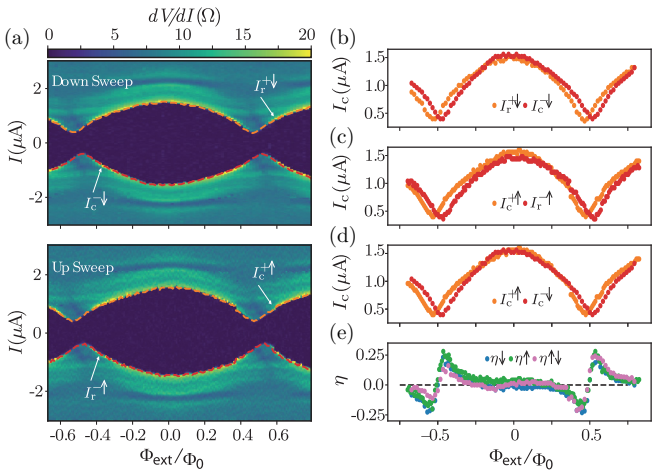

FIG. 6. (a) Two differential resistance plots of the SQUID device for the same gate settings as a function of external flux Φ_{ext} and current bias I. In the upper plot the current was swept downwards from positive to negative values, while in the lower it was swept upwards. Panels (b) and (c) compare the critical current values I_c with the retrapping ones I_r, obtained from (a) and (b) at the position of the peaks in dV/dI. The arrows ↑, ↓ indicate the sweep direction. Panel (d) compares $I_c^{+\uparrow}$ with $I_c^{-\downarrow}$, and in (e) the diode efficiency is shown for three ways using the data in (b)–(d).

setup sources a current using a 1 MΩ resistor in series to a dc voltage source on which a small ac component with frequency $f = 17.7$ Hz, supplied by a lock-in amplifier, is superposed. This current is applied to the source contact of the SQUID on the left with the drain contact on the right side galvanically connected to ground. The SQUID is shunted at the source to ground with a resistor $R_S = 10$ Ω. This shunt resistor is directly placed on the sample holder. In addition, a finger capacitance of ≈0.7 pF is patterned in parallel to the SQUID (lower right of the optical image). The original purpose of the capacitance was to increase the quality factor of the Josephson junctions. However, its effect is negligible, since the capacitance provided by the leads is larger. We measure the differential resistance of the shunted device using a voltage amplifier and lock-in techniques. The flux through the SQUID is generated by a vector magnet.

APPENDIX B: ESTIMATION OF LOOP INDUCTANCES

In the following we will detail the evaluation of the inductance of the loop branches. The loop geometry is defined as indicated by the white dashed lines in Fig. 5(a). The width of the two branches corresponds to the junctions width in the upper and lower path, $W_1 = 3$ μm, $W_2 = 2.5$ μm, and the width on the left and right sides it is set equal to $W_L = (W_1 + W_2)/2 = 2.75$ μm. In reality there is no lateral confinement in the superconductor. Hence, the artificial confinement increases the inductance values so that the simulated inductances for this geometry yield upper bounds to the inductances of the device. With finite-element simulations performed in Sonnet, we compute the two-port impedances $Z_{i,k}$ with i,k ∈ {1, 2} for different frequencies. The impedance is evaluated between two sets of floating co-calibrated ports, positioned on the left and right side of the loop. In the simulation we use InP as a substrate, with a relative dielectric constant $\epsilon_r = 12.4$.

The kinetic inductance of the Al film is evaluated by measuring the temperature dependence of the resistance of an Al bar realized on a different chip from the same wafer. We measure a critical temperature of 1.25 K and a normal state resistance of 15.5 Ω. The kinetic sheet inductance $L_{kin/\square}$ is then obtained through the low frequency limit of the Mattis-Bardeen screening theory [72–74]:

$$L_{kin/\square} = \frac{\hbar R_{n/\square}}{\pi \Delta_0} \tanh^{-1}\left(\frac{\Delta_0}{2k_B T}\right). \tag{B1}$$

Here $R_{n/\square}$ is the normal state sheet resistance, Δ_0 the zero-temperature BCS gap, and T the absolute temperature. Using Eq. (B1) we extract $L_{kin/\square} \approx 5$nH.

APPENDIX C: RETRAPPING VERSUS SWITCHING CURRENT

In Fig. 6 we compare the switching current with the retrapping current values. We show that the two values coincide in this experiment to a good accuracy. On our opinion this is due to the low parallel resistor, which keeps the voltage over the junction small in the normal state, hence, reducing overheating effects. Additionally, the shunt resistor adds damping at the plasma frequency of the junctions, which reduces the quality factor.

The two measurements in Fig. 6(a) were obtained for exactly the same parameter settings, except for the direction of current-bias sweep. In the upper (lower) measurement the current was decreased (increased) starting with positive (negative) values at +3 μA (−3 μA) and sweeping down (up) to −3 μA (+3 μA). Figure 6(b) shows the critical and retrapping current, I_c and I_r, extracted from the down-sweep data at positions where the differential resistance shows a peak.

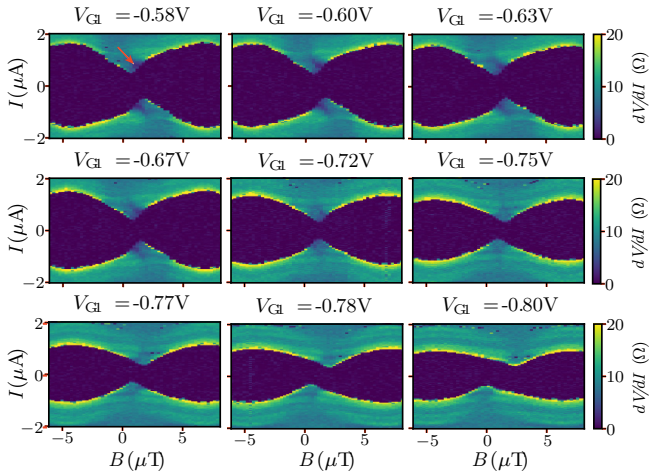

FIG. 7. SQUID oscillation at different gate voltage configurations. V_{G2} is fixed at -0.5 V, while V_{G1} is swept from -0.57 V to -0.8 V. The asymmetry in the SQUID oscillations follows the asymmetry in critical current between the two junctions. We have $I_{c1}(V_{G1} = -0.57\,V) > I_{c2}(V_{G2} = -0.5\,V)$ and $I_{c1}(V_{G1} = -0.8\,V) < I_{c2}(V_{G2} = -0.5\,V)$.

Figure 6(c) shows the same, but extracted from the up-sweep data. On sweeping downwards, we denote the negative critical current as $I_c^{-\downarrow}$ and the positive retrapping current as $I_r^{+\downarrow}$. In analogy, on sweeping upwards, the positive critical current is denoted by $I_c^{+\uparrow}$ and the negative retrapping current by $I_r^{-\uparrow}$. In Fig. 6(d) we compare the positive and negative critical currents, both obtained in a proper way using oppositive sweep directions.

Now we can compare the extracted diode efficiency for three cases: (1) for the case when we extract the critical currents from sweeping the current bias into negative direction only, $\eta^{\downarrow}$, (2) into the positive direction only, $\eta^{\uparrow}$, and (3) when we deduce the critical current properly, $\eta^{\uparrow\downarrow}$. The three curves are directly obtained from Figs. 6(b)–6(d). All three methods yield qualitatively the same efficiencies with no significant differences. Importantly, one clearly cannot say that $\eta^{\uparrow\downarrow}$ would yield in general lower efficiencies.

APPENDIX D: SQUID OSCILLATIONS AT DIFFERENT GATE VOLTAGES

In this Appendix we show how the SQUID pattern develops when the critical current of one junction is tuned from being larger, equal, and finally smaller than the critical current of the other junction. Figure 7 shows the differential resistance of the SQUID as a function of current bias and perpendicular magnetic field. V_{G2} is fixed at -0.5 V, while V_{G1} is swept from -0.57 V to -0.8 V. As extracted from Fig. 1(c), $I_{c2}(V_{G2} = -0.5) \sim 720$ nA, while $I_{c1}(V_{G1} = -0.57) \sim 1.12$ μA and $I_{c1}(V_{G1} = -0.8) \sim 360$ nA (gate voltages are given in units of V).

The sign of the diode efficiency is mirrored with respect to the magnetic field value corresponding to half flux quantum when the critical current asymmetry α between the two junctions changes sign. We also notice a dip in differential resistance developing around half flux quantum that evolves with α (see arrow in Fig. 7).

APPENDIX E: MODEL INCLUDING LOOP INDUCTANCES

As introduced in the main text, we model the current-phase relation of a single junction i ∈ [1, 2] with

$$I_i(\varphi_1) = \frac{N_i \tau_i^* e\Delta}{\hbar} \frac{\sin(\varphi_i)}{\sqrt{1 - \tau_i^* \sin^2(\varphi_i/2)}}, \tag{E1}$$

where N_i stands for the number of channels and τ_i^* for an effective transmission probability of junction i. The more general approach would be to assume a distribution function for the transmission probability of each channel. To avoid this complication we assume that all channels have the same transmission probability τ_i^*.

We introduce the normalization parameter A_i as

$$A_i := \max_{\varphi_i} \left\{ \frac{\sin(\varphi_i)}{\sqrt{1 - \tau_i^* \sin^2(\varphi_i)}} \right\}. \tag{E2}$$

Note that A_i depends only on τ_i^*. We thus get the normalized CPR as

$$I_i(\varphi_i) = \frac{I_{ci}}{A_i} \frac{\sin(\varphi_i)}{\sqrt{1 - \tau_i^* \sin^2(\varphi_i/2)}}. \tag{E3}$$

In this notation of the CPR, N has been replaced by the critical current I_c, which appears now explicitly.

Flux quantization in the loop imposes

$$\varphi_1 - \varphi_2 = 2\pi\,\Phi/\Phi_0. \tag{E4}$$

Here the total flux in the loop Φ is given by the external flux Φ_{ext} and the contributions from the screening currents expressed through the loop inductances, L_1 and L_2, that belong to the two branches. If mutual inductances are considered too, one has to introduce new effective inductances $L_1' = L_1 - M$ and $L_2' = L_2 - M$, where M describes the mutual inductance. We obtain for the total flux

$$\Phi = \Phi_{ext} - L_1' I_1(\varphi_1) + L_2' I_2(\varphi_2). \tag{E5}$$

Therefore, Eq. (E4) now reads

$$\varphi_1 - \varphi_2 = \varphi_{ext} + \frac{2\pi}{\Phi_0}[L_2' I_2(\varphi_2) - L_1' I_1(\varphi_1)]. \tag{E6}$$

Our simulations show, however, that the effect of the mutual inductance can be neglected in our experiment. Hence, there are six remaining parameters in the problem: I_{c1}, I_{c2}, τ_1^*, τ_2^*, L_1, and L_2. Since the appearance of the SDE in a SQUID is related to asymmetries, we introduce three asymmetry parameters:

$$\alpha := \frac{I_{c1} - I_{c2}}{I_{c1} + I_{c2}}, \tag{E7}$$

$$\beta := \frac{\tau_1^* - \tau_2^*}{\tau_1^* + \tau_2^*}, \tag{E8}$$

$$\gamma := \frac{L_1 - L_2}{L_1 + L_2}. \tag{E9}$$

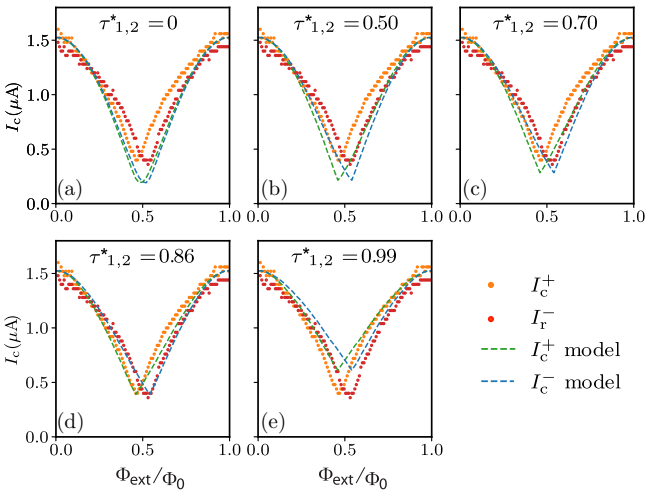

FIG. 8. Sequence of simulations for I_c^+ (green dashed curves) and I_c^- (blue dashed curves) to measured (up-sweep) data I_c^+ (orange dots) and I_r^- (red dots). In (a) a sinusoidal CPR with the estimated loop inductance asymmetry is considered, while in graphs (b)–(e) the effective transparencies τ^* of the junctions ar increased. Further details are given in the text.

The new set of parameters is now given by the three asymmetries and the average values of the two junctions for the critical current $\bar{I}_c$, the transmission probability $\bar{\tau}$, and the inductance $\bar{L}$.

To find the critical current one has to find the maximum or minimum of the total supercurrent:

$$I(\varphi_1, \varphi_2) = I_1(\varphi_1) + I_2(\varphi_2). \tag{E10}$$

Making use of Eq. (E6), we get

$$I(\varphi_1, I) = I_1(\varphi_1) + I_2\{\varphi_1 - \varphi_{ext} + \kappa L_1 I_1(\varphi_1) - \kappa L_2[I - I_1(\varphi_1)]\}, \tag{E11}$$

with $\kappa = 2\pi/\Phi_0$. In the latter form, we have eliminated φ_2 using the fluxoid condition. However, due to the loop inductances, the equation for the total current I is now itself implicitly dependent on I. One can still solve this equation recursively or by introducing Lagrange multipliers to then search for the maximum or minimum currents, yielding I_c^+ and I_c^- [64].

To find I_c^+ numerically, we preset the value of I, $0 \leqslant I \leqslant 2\bar{I}_c$, starting with a small one and search for solutions φ_1 of Eq. (E11). If solutions exist, we increment I by a small step δI until there are no solutions φ_1 anymore. This defines I_c^+. In analogy we obtain I_c^-.

APPENDIX F: COMPARISON TO DIODE EFFECT DUE TO LOOP INDUCTANCES

Here we present a comparison of the measured critical currents I_c^+ and I_c^- shown in Fig. 2(c) with model simulations. Specifically, we discuss the effect of the loop inductance and its asymmetry on the SDE. The comparison shows that the SDE can poorly be reproduced taking only the loop inductances into account. This is shown in Fig. 8.

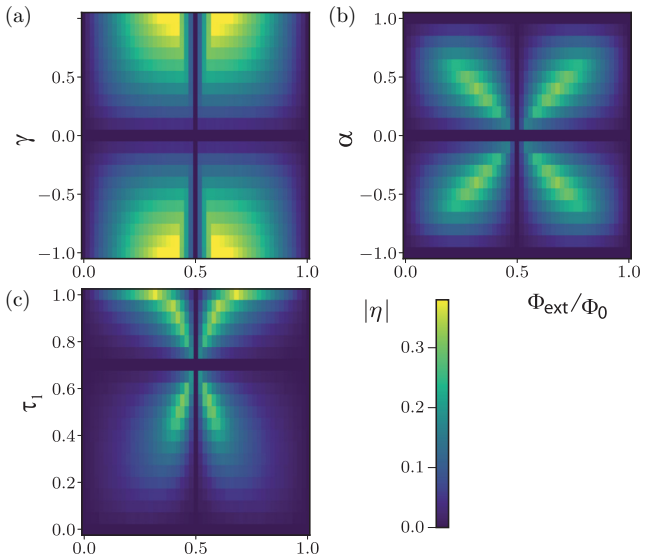

FIG. 9. Magnitude of the diode efficiency $|\eta|$ as a function of the applied external flux Φ_{ext} expressed in number of magnetic flux quanta Φ_0, numerically calculated for a SQUID with two sinusoidal CPRs with an asymmetry (a) in loop inductance γ and (b) in critical current α. The inductances were chosen such that $\varphi_L = \pi$. In (c) $|\eta|$ is plotted for a SQUID without loop inductances and two JJs, each with a nonsinusoidal single-channel CPR, as a function of τ_1 and normalized external flux for $\tau_2 = 0.7$ and for $\alpha = \gamma = \varphi_L = 0$.

Figure 8 shows a sequence of simulations, blue and green dashed curves, to a set of measurements of I_c^+ (orange) and I_r^- (red). In all five simulations the critical currents I_{c1} and I_{c2} of the two junctions are taken from the experiment, from Fig. 1(c). Since $V_{G1} = V_{G2} = 0$ we obtain $I_{c1} = 0.87$ μA and $I_{c2} = 0.67$ μA. In Fig. 8(a) we assume sinusoidal CPRs for both junctions JJ_1 and JJ_2, and we take the simulated loop inductances into account. Due to the slight asymmetry in loop inductance a small SDE appears. However, this effect is far smaller than what has been measured. Hence, one cannot fit the measurement with the loop inductance asymmetry alone. In Figs. 8(b)–8(e) we keep the loop inductances as estimated, but change to nonsinusoidal CPRs by increasing $\tau_1^* = \tau_2^*$ to appreciable values ranging 0.5–0.99, indicated in the figures. As before, we obtain the blue and green dashed curves taking the known critical currents I_{c1} and I_{c2} of the two junctions. The best match in this sequence is found for $\tau_1^* = \tau_2^* \approx 0.86$. One can see that the model matches the key features of the experiment very well. However, there are deviations, as seen by the stronger curvature that the measurement points display as compared to the model. The model assumes an almost triangular shape for very large transparencies $\tau_1^* = \tau_2^* \approx 0.99$ These differences are yet not understood

APPENDIX G: CONDITIONS FOR A DIODE EFFECT IN A SQUID DEVICE

Figure 9 illustrates that an asymmetry is required to obtain a SDE. in Figs. 9(a) and 9(b) sinusoidal CPRs are assumed. In Fig. 9(a) the loop inductance asymmetry γ

TABLE II. Conditions for obtaining a superconducting diode-effect (SDE). In the first column $\tau^* = 0$ is used to refer to a sinusoidal CPR, while $\tau^* \neq 0$ indicates a highly transmissive CPR containing higher order terms in the CPR. If $\bar{L} = 0$, loop inductances are not considered, while they play a role in the entries where $\bar{L} \neq 0$. α (β) denotes the asymmetry in I_c (τ^*) of the two JJs, while γ denotes the asymmetry in the loop inductances in the two arms of the SQUID.

τ^*	β	α	$\bar{L}$	γ	SDE
0	n.a.	0	0	n.a.	No
0	n.a.	0	$\neq 0$	0	No
0	n.a.	0	$\neq 0$	$\neq 0$	Yes
0	n.a.	$\neq 0$	0	n.a.	No
0	n.a.	$\neq 0$	$\neq 0$	0	Yes
0	n.a.	$\neq 0$	$\neq 0$	$\neq 0$	Yes
$\neq 0$	0	0	0	n.a.	No
$\neq 0$	0	0	$\neq 0$	0	No
$\neq 0$	0	0	$\neq 0$	$\neq 0$	Yes
$\neq 0$	0	$\neq 0$	0	n.a.	Yes
$\neq 0$	0	$\neq 0$	$\neq 0$	0	Yes
$\neq 0$	0	$\neq 0$	$\neq 0$	$\neq 0$	Yes
$\neq 0$	$\neq 0$	0	0	n.a.	Yes
$\neq 0$	$\neq 0$	0	$\neq 0$	0	Yes
$\neq 0$	$\neq 0$	0	$\neq 0$	$\neq 0$	Yes
$\neq 0$	$\neq 0$	$\neq 0$	0	n.a.	Yes
$\neq 0$	$\neq 0$	$\neq 0$	$\neq 0$	0	Yes
$\neq 0$	$\neq 0$	$\neq 0$	$\neq 0$	$\neq 0$	Yes

is varied, while the critical-current asymmetry $\alpha = 0$. In contrast, in Fig. 9(b) α is varied, while $\gamma = 0$. The loop inductance has been chosen such that the average phase drop over the inductor $\varphi_L = 4\pi \bar{I}_c \bar{L} \Phi_0$ assumes a large value of $\varphi_L = \pi$. In Fig. 9(c) a SQUID with two single-channel nonsinusoidal CPRs with different transmission probabilities $\tau_{1,2} \neq 0$ (asymmetry $\beta \neq 0$) are considered, while $\alpha = \gamma = \varphi_L = 0$.

In general, it is seen that the diode efficiency is zero at the symmetry points corresponding in Fig. 9(a) to $\gamma = 0$, in Fig. 9(b) to $\alpha = 0$, and in Fig. 9(c) to $\tau_1 = \tau_2$. Further, $\eta = 0$ for $\varphi_{ext} = 2\pi \Phi_{ext}/\Phi_0 = 0, \pi$, and 2π. For these cases one can show that the CPR of the SQUID is odd in the phase difference φ. This follows from Eq. (5) and the fact that $I_1(\varphi)$ and $I_2(\varphi)$ are odd functions in φ. In addition, we note that the position of maximum diode efficiency in flux depends on what kind of asymmetry dominates. It can take values >30%.

To obtain a SDE in a SQUID loop, an asymmetry is required. This we have illustrated in Fig. 9, where out of the three asymmetry parameters α, β, γ only one was different from zero. In Table II we show under which conditions the SDE appears depending on all three asymmetry parameters. The table shows that at least one symmetry has to be broken to get the SDE effect. This is a sufficient condition for almost all cases. There is only one exception. It arises for sinusoidal CPRs where a difference in critical currents of the two junctions is not enough for a SDE to appear.

[1] T. H. Kokkeler, A. A. Golubov, and F. S. Bergeret, Field-free anomalous junction and superconducting diode effect in spin-split superconductor/topological insulator junctions, Phys. Rev. B **106**, 214504 (2022).

[2] Y. Zhang, Y. Gu, P. Li, J. Hu, and K. Jiang, General Theory of Josephson Diodes, Phys. Rev. X **12**, 041013 (2022).

[3] B. Josephson, Possible new effects in superconductive tunnelling, Phys. Lett. **1**, 251 (1962).

[4] A. A. Golubov, M. Y. Kupriyanov, and E. Il'ichev, The current-phase relation in Josephson junctions, Rev. Mod. Phys. **76**, 411 (2004).

[5] M. C. Koops, G. V. van Duyneveldt, and R. de Bruyn Ouboter, Direct Observation of the Current-Phase Relation of an Adjustable Superconducting Point Contact, Phys. Rev. Lett. **77**, 2542 (1996).

[6] M. L. DellaRocca, M. Chauvin, B. Huard, H. Pothier, D. Esteve, and C. Urbina, Measurement of the Current-Phase Relation of Superconducting Atomic Contacts, Phys. Rev. Lett. **99**, 127005 (2007).

[7] A. I. Buzdin, L. N. Bulaevskii, and S. V. Panyukov, Critical-current oscillations as a function of the exchange field and thickness of the ferromagnetic metal (F) in an S-F-S Josephson junction, Pis'ma Zh. Eksp. Teor. Fiz. **35**, 147 (1982) [JETP Lett. **35**, 178 (1982)].

[8] A. Buzdin, π-junction realization due to tunneling through a thin ferromagnetic layer, JEPT Lett. **78**, 583 (2003).

[9] V. V. Ryazanov, V. A. Oboznov, A. Y. Rusanov, A. V. Veretennikov, A. A. Golubov, and J. Aarts, Coupling of Two Superconductors through a Ferromagnet: Evidence for a π Junction, Phys. Rev. Lett. **86**, 2427 (2001).

[10] T. Kontos, M. Aprili, J. Lesueur, F. Genêt, B. Stephanidis, and R. Boursier, Josephson Junction through a Thin Ferromagnetic Layer: Negative Coupling, Phys. Rev. Lett. **89**, 137007 (2002).

[11] E. C. Gingrich, B. M. Niedzielski, J. A. Glick, Y. Wang, D. L. Miller, R. Loloee, W. P. P. Jr, and N. O. Birge, Controllable π Josephson junctions containing a ferromagnetic spin valve, Nat. Phys. **12**, 564 (2016).

[12] H. Sickinger, A. Lipman, M. Weides, R. G. Mints, H. Kohlstedt, D. Koelle, R. Kleiner, and E. Goldobin, Experimental Evidence of a ϕ Josephson Junction, Phys. Rev. Lett. **109**, 107002 (2012).

[13] I. V. Krive, L. Y. Gorelik, R. I. Shekhter, and M. Jonson, Chiral symmetry breaking and the Josephson current in a ballistic superconductor-quantum wire-superconductor junction, Low Temp. Phys. **30**, 398 (2004).

[14] A. A. Reynoso, G. Usaj, C. A. Balseiro, D. Feinberg, and M. Avignon, Anomalous Josephson Current in Junctions with Spin Polarizing Quantum Point Contacts, Phys. Rev. Lett. **101**, 107001 (2008).

[15] A. Buzdin, Direct Coupling between Magnetism and Superconducting Current in the Josephson ϕ_0 Junction, Phys. Rev. Lett. **101**, 107005 (2008).

[16] A. Zazunov, R. Egger, T. Jonckheere, and T. Martin, Anomalous Josephson Current through a Spin-Orbit Coupled Quantum Dot, Phys. Rev. Lett. **103**, 147004 (2009).

[17] T. Yokoyama, M. Eto, and Y. V. Nazarov, Josephson current through semiconductor nanowire with spin–orbit interaction in magnetic field, J. Phys. Soc. Jpn. **82**, 054703 (2013).

[18] R. Wakatsuki, Y. Saito, S. Hoshino, Y. M. Itahashi, T. Ideue, M. Ezawa, Y. Iwasa, and N. Nagaosa, Nonreciprocal charge

transport in noncentrosymmetric superconductors, Sci. Adv. **3**, e1602390 (2017).

[19] B. Turini, S. Salimian, M. Carrega, A. Iorio, E. Strambini, F. Giazotto, V. Zannier, L. Sorba, and S. Heun, Josephson diode effect in high-mobility InSb nanoflags, Nano Lett. **22**, 8502 (2022).

[20] D. B. Szombati, S. Nadj-Perge, D. Car, S. R. Plissard, E. P. A. M. Bakkers, and L. P. Kouwenhoven, Josephson ϕ_0-junction in nanowire quantum dots, Nat. Phys. **12**, 568 (2016).

[21] C. B. L. Fuchs, A. Costa, J. J. Pico-Cortes, S. Reinhardt, S. Gronin, G. C. Gardner, T. Lindemann, M. J. Manfra, P. E. F. Junior, D. Kochan *et al.*, Effect of Rashba and Dresselhaus spin-orbit coupling on supercurrent rectification and magnetochiral anisotropy of ballistic Josephson junctions, J. Phys.-Conden. Matter C **34**, 154005 (2022).

[22] G. L. J. A. Rikken, J. Fölling, and P. Wyder, Electrical Magnetochiral Anisotropy, Phys. Rev. Lett. **87**, 236602 (2001).

[23] G. L. J. A. Rikken and P. Wyder, Magnetoelectric Anisotropy in Diffusive Transport, Phys. Rev. Lett. **94**, 016601 (2005).

[24] F. Ando, Y. Miyasaka, T. Li, J. Ishizuka, T. Arakawa, Y. Shiota, T. Moriyama, Y. Yanase, and T. Ono, Observation of superconducting diode effect, Nature (London) **584**, 373 (2020).

[25] A. Daido, Y. Ikeda, and Y. Yanase, Intrinsic Superconducting Diode Effect, Phys. Rev. Lett. **128**, 037001 (2022).

[26] C. Baumgartner, L. Fuchs, A. Costa, S. Reinhardt, S. Gronin, G. C. Gardner, T. Lindemann, M. J. Manfra, P. F. F. Junior, D. Kochan *et al.*, Supercurrent rectification and magnetochiral effects in symmetric Josephson junctions, Nat. Nanotechnol. **17**, 39 (2022).

[27] L. Bauriedl, C. Bäuml, L. Fuchs, C. Baumgartner, N. Paulik, J. M. Bauer, K.-Q. Lin, J. M. Lupton, T. Taniguchi, K. Watanabe *et al.*, Supercurrent diode effect and magnetochiral anisotropy in few-layer $NbSe_2$, Nat. Commun. **13**, 4266 (2022).

[28] H. Narita, J. Ishizuka, R. Kawarazaki, D. Kan, Y. Shiota, T. Moriyama, Y. Shimakawa, V. A. Ognev, A. S. Samardak, Y. Yanase, and T. Ono, Field-free superconducting diode effect in noncentrosymmetric superconductor/ferromagnet multilayers, Nat. Nanotechnol. **17**, 823 (2022).

[29] K.-R. Jeon, J.-K. Kim, J. Yoon, J.-C. Jeon, H. Han, A. Cottet, T. Kontos, and S. P. Parkin, Zero-field polarity-reversible Josephson supercurrent diodes enabled by a proximity magnetized Pt barrier, Nat. Mater. **21**, 1211 (2022).

[30] H. Wu, Y. Wang, Y. Xu, P. K. Sivakumar, C. Pasco, U. Filippozzi, S. S. P. Parkin, Y.-J. Zeng, T. McQueen, and M. N. Ali, The field-free Josephson diode in a van der Waals heterostructure, Nature (London) **604**, 653 (2022).

[31] J.-X. Lin, P. Siriviboon, H. D. Scammell, S. Liu, D. Rhodes, K. Watanabe, T. Taniguchi, J. Hone, M. S. Scheurer, and J. I. A. Li, Zero-field superconducting diode effect in small-twist-angle trilayer graphene, Nat. Phys. **18**, 1221 (2022).

[32] J. Diez-Merida, A. Diez-Carlon, S. Y. Yang, Y.-M. Xie, X.-J. Gao, J. Senior, K. Watanabe, T. Taniguchi, X. Lu, A. P. Higginbotham *et al.*, Symmetry-broken Josephson junctions and superconducting diodes in magic-angle twisted bilayer graphene, Nat. Commun. **14**, 2396 (2023).

[33] N. F. Q. Yuan and L. Fu, Supercurrent diode effect and finite-momentum superconductors, Proc. Nat. Acad. Sci. USA **119**, e2119548119 (2022).

[34] M. Davydova, S. Prembabu, and L. Fu, Universal Josephson diode effect, Sci. Adv. **8**, eabo0309 (2022).

[35] D. Suri, A. Kamra, T. N. G. Meier, M. Kronseder, W. Belzig, C. H. Back, and C. Strunk, Non-reciprocity of vortex-limited critical current in conventional superconducting micro-bridges, Appl. Phys. Lett. **121**, 102601 (2022).

[36] B. Pal, A. Chakraborty, P. K. Sivakumar, M. Davydova, A. K. Gopi, A. K. Pandeya, J. A. Krieger, Y. Zhang, M. Date, S. Ju *et al.*, Josephson diode effect from Cooper pair momentum in a topological semimetal, Nat. Phys. **18**, 1228 (2022).

[37] M. Trahms, L. Melischek, J. F. Steiner, B. Mahendru, I. Tamir, N. Bogdanoff, O. Peters, G. Reecht, C. B. Winkelmann, and F. von Oppenand K. J. Franke, Diode effect in Josephson junctions with a single magnetic atom, Nature (London) **615**, 628 (2023).

[38] C.-Z. Chen, J. J. He, M. N. Ali, G.-H. Lee, K. C. Fong, and K. T. Law, Asymmetric Josephson effect in inversion symmetry breaking topological materials, Phys. Rev. B **98**, 075430 (2018).

[39] A. Kononov, G. Abulizi, K. Qu, J. Yan, D. Mandrus, K. Watanabe, T. Taniguchi, and C. Schönenberger, One-dimensional edge transport in few-layer WTe_2, Nano Lett. **20**, 4228 (2020).

[40] H. F. Legg, D. Loss, and J. Klinovaja, Superconducting diode effect due to magnetochiral anisotropy in topological insulators and Rashba nanowires, Phys. Rev. B **106**, 104501 (2022).

[41] J. J. Cuozzo, W. Pan, J. Shabani, and E. Rossi, Microwave-tunable diode effect in asymmetric squids with topological Josephson junctions, arXiv:2303.16931.

[42] T. A. Fulton and R. C. Dynes, Current-Phase Relations in Superconducting Bridges, Phys. Rev. Lett. **25**, 794 (1970).

[43] T. A. Fulton, L. N. Dunkleberger, and R. C. Dynes, Quantum interference properties of double Josephson junctions, Phys. Rev. B **6**, 855 (1972).

[44] W.-T. Tsang and T. V. Duzer, dc analysis of parallel arrays of two and three Josephson junctions, J. Appl. Phys. **46**, 4573 (1975).

[45] A. Barone and G. Paterno, *Physics and Applications of the Josephson Effect* (John Wiley & Sons, New York, 1982).

[46] M. R. Buitelaar, T. Nussbaumer, and C. Schönenberger, Quantum Dot in the Kondo Regime Coupled to Superconductors, Phys. Rev. Lett. **89**, 256801 (2002).

[47] Y.-J. Doh, J. A. van Dam, A. L. Roest, E. P. A. M. Bakkers, L. P. Kouwenhoven, and S. D. Franceschi, Tunable supercurrent through semiconductor nanowires, Science **309**, 272 (2005).

[48] T. W. Larsen, K. D. Petersson, F. Kuemmeth, T. S. Jespersen, P. Krogstrup, J. Nygård, and C. M. Marcus, Semiconductor-Nanowire-Based Superconducting Qubit, Phys. Rev. Lett. **115**, 127001 (2015).

[49] E. Prada, P. San-Jose, M. W. A. de Moor, A. Geresdi, E. J. H. Lee, J. Klinovaja, D. Loss, J. Nygård, R. Aguado, and L. P. Kouwenhoven, From Andreev to Majorana bound states in hybrid superconductor-semiconductor nanowires, Nat. Rev. Phys. **2**, 575 (2020).

[50] G. Burkard, M. J. Gullans, X. Mi, and J. R. Petta, Superconductor-semiconductor hybrid-circuit quantum electrodynamics, Nat. Rev. Phys. **2**, 129 (2020).

[51] R. S. Souto, M. Leijnse, and C. Schrade, Josephson Diode Effect in Supercurrent Interferometers, Phys. Rev. Lett. **129**, 267702 (2022).

[52] Y. V. Fominov and D. S.Mikhailov, Asymmetric higher-harmonic SQUID as a Josephson diode, Phys. Rev. B **106**, 134514 (2022).

[53] J. S. Lee, B. Shojaei, M. Pendharkar, A. P. McFadden, Y. Kim, H. J. Suominen, M. Kjaergaard, F. Nichele, H. Zhang, C. M. Marcus, and C. J. Palmstrøm, Transport studies of Epi-Al/InAs two-dimensional electron gas systems for required building-blocks in topological superconductor networks, Nano Lett. **19**, 3083 (2019).

[54] F. Nichele, E. Portolés, A. Fornieri, A. M. Whiticar, A. C. C. Drachmann, S. Gronin, T. Wang, G. C. Gardner, C. Thomas, A. T. Hatke *et al.*, Relating Andreev Bound States and Supercurrents in Hybrid Josephson Junctions, Phys. Rev. Lett. **124**, 226801 (2020).

[55] O. Dorokhov, On the coexistence of localized and extended electronic states in the metallic phase, Solid State Commun. **51**, 381 (1984).

[56] G. Nanda, J. L. Aguilera-Servin, P. Rakyta, A. Kormányos, R. Kleiner, D. Koelle, K. Watanabe, T. Taniguchi, L. M. K. Vandersypen, and S. Goswami, Current-phase relation of ballistic graphene Josephson junctions, Nano Lett. **17**, 3396 (2017).

[57] L. Bretheau, J. I.-J. Wang, R. Pisoni, K. Watanabe, T. Taniguchi, and P. Jarillo-Herrero, Tunnelling spectroscopy of Andreev states in graphene, Nat. Phys. **13**, 756 (2017).

[58] D. A. Manjarrés, S. Gomez Páez, and W. J. Herrera, Skewness and critical current behavior in a graphene Josephson junction, Phys. Rev. B **101**, 064503 (2020).

[59] D. I. Indolese, P. Karnatak, A. Kononov, R. Delagrange, R. Haller, L. Wang, P. Makk, K. Watanabe, T. Taniguchi, and C. Schönenberger, Compact squid realized in a double-layer graphene heterostructure, Nano Lett. **20**, 7129 (2020).

[60] R. Haller, G. Fülöp, D. Indolese, J. Ridderbos, R. Kraft, L. Y. Cheung, J. H. Ungerer, K. Watanabe, T. Taniguchi, D. Beckmann *et al.*, Phase-dependent microwave response of a graphene Josephson junction, Phys. Rev. Res. **4**, 013198 (2022).

[61] I. O. Kulik and A. N. Omel'yanchuk, Contribution to the microscopic theory of the Josephson effect in superconducting bridges, Pis'ma Zh. Eksp. Teor. Fiz. **21**, 216 (1975) [JETP Lett. **21**, 96 (1975)].

[62] Y. V. Nazarov, Limits of Universality in Disordered Conductors, Phys. Rev. Lett. **73**, 134 (1994).

[63] C. W. J. Beenakker, Random-matrix theory of quantum transport, Rev. Mod. Phys. **69**, 731 (1997).

[64] C. D. Tesche and J. Clarke, dc SQUID: Noise and optimization, J. Low Temp. Phys. **29**, 301 (1977).

[65] J. Clarke and A. I. Braginski (eds.), *The SQUID Handbook, Fundamentals and Technology of SQUIDs and SQUID Systems,*, Vol. I (Wiley-VCH Verlag, Weinheim, Germany, 2004).

[66] C. Granata and A. Vettoliere, Nano superconducting quantum interference device: A powerful tool for nanoscale investigations, Phys. Rep. **614**, 1 (2016).

[67] L. Tosi, C. Metzger, M. F. Goffman, C. Urbina, H. Pothier, S. Park, A. L. Yeyati, J. Nygard, and P. Krogstrup, Spin-Orbit Splitting of Andreev States Revealed by Microwave Spectroscopy, Phys. Rev. X **9**, 011010 (2019).

[68] F. Paolucci, G. D. Simoni, and F. Giazotto, A gate- and flux-controlled supercurrent diode effect, Appl. Phys. Lett. **122**, 042601 (2023).

[69] M. Gupta, G. V. Graziano, M. Pendharkar, J. T. Dong, C. P. Dempsey, C. Palmstrøm, and V. S. Pribiag, Gate-tunable superconducting diode effect in a three-terminal Josephson device, Nat. Commun. **14**, 3078 (2023).

[70] M. Valentini, O. Sagi, L. Baghumyan, T. de Gijsel, J. Jung, S. Calcaterra, A. Ballabio, J. A. Servin, K. Aggarwal, M. Janik *et al.*, Radio frequency driven superconducting diode and parity conserving Cooper pair transport in a two-dimensional germanium hole gas, arXiv:2306.07109.

[71] https://doi.org/10.5281/zenodo.7733057.

[72] D. C. Mattis and J. Bardeen, Theory of the anomalous skin effect in normal and superconducting metals, Phys. Rev. **111**, 412 (1958).

[73] M. Tinkham, *Introduction to Superconductivity*, 2nd ed. (Dover Publications, New York, 2004).

[74] A. J. Annunziata, D. F. Santavicca, L. Frunzio, G. Catelani, M. J. Rooks, A. Frydman, and D. E. Prober, Tunable superconducting nanoinductors, Nanotechnology **21**, 445202 (2010).